PHYSICAL REVIEW B VOLUME 62, NUMBER 5 1 AUGUST 2000-I

Enhancement of perpendicular and parallel giant magnetoresistance with the number of bilayers in Fe/Cr superlattices

M. C. Cyrille,[1] S. Kim,[1] M. E. Gomez,[1,*] J. Santamaria,[1,†] Kannan M. Krishnan,[2] and Ivan K. Schuller[1]
[1]*Department of Physics, University of California-San Diego, La Jolla, California 92093-0319*
[2]*Materials Sciences Division, National Center for Electron Microscopy, Lawrence Berkeley Laboratory, University of California, Berkeley, California 94720*
(Received 28 December 1999)

We have correlated a detailed quantitative structural analysis by x-ray diffraction, transmission electron microscopy, and high spatial resolution electron energy-loss spectroscopy imaging, with the magnetization and anisotropic magnetotransport properties in sputtered Fe/Cr superlattices. To accomplish this, we developed a technique for magnetotransport measurements in metallic superlattices with the current perpendicular to the plane of the layers (CPP). Using microfabrication techniques, we have fabricated microstructured Fe/Cr pillars embedded in SiO_2 and interconnected with Nb electrodes. Because of the uniform current distribution in the Nb electrodes and the minimization of the superlattice-electrode contact resistance, the method allows a simple and independent measurement of the superlattice resistance and giant magnetoresistance (GMR). Structural and magnetic characterization of $[\mathrm{Fe}\,(3\,\mathrm{nm})/\mathrm{Cr}\,(1.2\,\mathrm{nm})]_N$ superlattices (where N is the number of repetitions) indicate that the roughness is correlated and increases cumulatively through the superlattice stack with no significant change in the antiferromagnetic coupling. Both the current in-plane and CPP GMR increase with N as the roughness increases.

I. INTRODUCTION

Since the discovery of giant magnetoresistance (GMR) in magnetic superlattices,[1] much interesting experimental and theoretical work has been done to understand this phenomenon. The GMR amplitude depends on several physical properties: the magnetic structure (via the interlayer exchange coupling), the spin dependent electronic band structure and the spin dependent electron scattering.[2–5] GMR measurements are usually carried out with a current in-plane (CIP) geometry, which is a straightforward technique. MR measurements in the current perpendicular to the plane (CPP) geometry are not easily achievable because of the small resistivity of the superlattices, although they allow the deconvolution of the electron scattering occurring in the ferromagnetic bulk from those occurring at the interfaces.[6,7] Several groups have developed methods to measure the CPP GMR in magnetic superlattices. Pratt *et al.*[8] developed a superconducting contacting technique together with a sensitive superconducting quantum interference device (SQUID) based system to measure the small resistance of their samples. Gijs, Lenczowski, and Giesbers[9] have measured the CPP GMR in Fe/Cr superlattices up to room temperature using microfabrication techniques with normal electrodes, Gijs *et al.*[10] and Ono and Shinjo[11] have used *V*-groove substrates to measure the GMR with the current at an angle to plane (CAP) geometry and Piraux *et al.*,[12] Blondel *et al.*,[13] and Liu *et al.*[14] have fabricated multilayered nanowires by electrodeposition.

We report on a different method to measure the magnetotransport properties of metallic superlattices in the CPP geometry. Using microfabrication techniques, we have fabricated microstructured pillars interconnected with Nb electrodes. This method's advantages are as follows: first, because of the high number of columns and their small cross section, the resistance of the sample is in the mΩ range which can be measured with conventional techniques. Second, because of the superconducting Nb electrodes, the current distribution is uniform in the pillars and computer simulation is not necessary to access the superlattice resistance.[9] Third, the contact resistance between the superlattice and the electrodes has been minimized. Because the smallest spurious contact resistance induced by the fabrication process will contribute to the measured resistance, this third point is the key to have independent access to the intrinsic superlattice resistance and magnetoresistance. Therefore, because the contact resistance is negligible, no adjustments or corrections have to be done to the measured resistance. Finally, this method can be applied to any superlattice system with no limitation on the layer thicknesses, provided that the saturation field is smaller than 1.2 T. We have used this method to determine the CIP and CPP magnetoresistance of $[\mathrm{Fe}\,(3\,\mathrm{nm})/\mathrm{Cr}\,(1.2\,\mathrm{nm})]_N$ superlattices, where N is the number of repetitions, grown by dc magnetron sputtering.

Because most of theoretical and experimental work underscore the importance of interfacial roughness, detailed structural characterization is critical to further understand the GMR. We have developed an interesting imaging technique using high-resolution electron energy-loss spectroscopy (EELS) in a transmission electron microscope (TEM) to *quantify* the interfacial roughness in metallic superlattices. Hence the superlattices interfacial disorder was characterized quantitatively using two complementary techniques: low-angle x-ray diffraction (LAXRD), and energy-filtered imaging using cross-section samples in an analytical TEM and was correlated with the superlattices magnetization and magnetotransport properties. LAXRD and EELS analysis of $[\mathrm{Fe}\,(3\,\mathrm{nm})/\mathrm{Cr}\,(1.2\,\mathrm{nm})]_N$ provide evidence that the roughness is correlated and increases cumulatively through the superlattice stack with no significant effect on the antiferro-

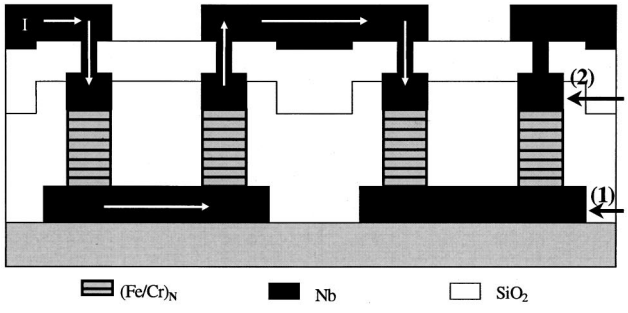

(a)

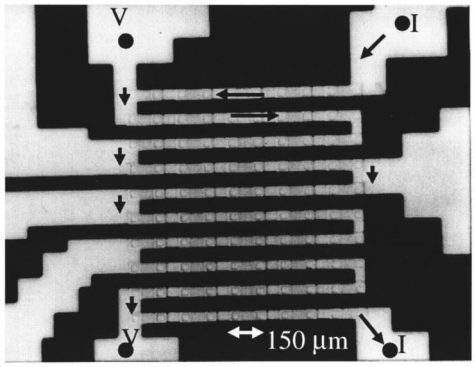

(b)

FIG. 1. (a) Schematic cross section of a CPP sample; arrows labeled (1) and (2) correspond to the patterns defined by the first and second etches, respectively; (b) optical micrograph of a typical sample. Arrows show the current path.

magnetic coupling. The current in plane (CIP) GMR and the current perpendicular to the plane (CPP) GMR were found to increase with N as the roughness increases cumulatively.

II. EXPERIMENTAL DESCRIPTION

A schematic cross section of the structure developed to measure the CPP resistance and magnetoresistance is given in Fig. 1(a). A Nb-superlattice-Nb sandwich is first deposited *in situ* by dc magnetron sputtering onto a Si substrate at room temperature. Both Nb layers are 100 nm thick and the superlattice consists of $[\mathrm{Fe}\,(3\,\mathrm{nm})/\mathrm{Cr}\,(1.2\,\mathrm{nm})]_N$. The Cr thickness has been chosen to correspond to the first antiferromagnetic (AF) coupling peak reported for polycrystalline (110) Fe/Cr superlattices.[15,16] The sandwich is then completely etched down to the substrate in the form of $50 \times 150\text{-}\mu\mathrm{m}^2$ pillars. The Nb is etched using reactive ion etching in a mixed CCl_2F_2 and O_2 atmosphere and the superlattices are etched with a mixture of HCI, H_3PO_4 and water. Then, only the top Nb layer and the superlattice are etched to form $30\times 30\text{-}\mu\mathrm{m}^2$ pillars. The pillars are embedded in a SiO_2 film deposited by rf magnetron sputtering and lifted off using the same photoresist mask. A second SiO_2 film is deposited by lift-off to complete the isolation and avoid any short circuit and a $10\times 10\,\mu\mathrm{m}^2$ via is defined on top of the columns. To prevent any parasitic contact resistance due to the oxidation of the top Nb layer during the lithography process, an ion milling step is performed and the first 10 nm of the Nb top layer is etched away. A final Nb layer is then immediately deposited *in situ* by molecular beam epitaxy (MBE) and patterned to form the connection between the pillars. When the Nb is superconducting, the current distribution in the Nb electrodes is uniform and the current flows perpendicular to the plane of the substrate inside the pillars. Figure 1(b) shows an optical micrograph of a typical sample. The sample consists of 100 pillars in series and has a ''meanderlike'' structure. Several contact pads can be used to perform a four-lead measurement.

To measure the resistance and magnetoresistance in the CIP configuration, the superlattices are deposited directly on top of a Si substrate. Then a 40-μm-wide bridge is defined using optical photolithography and the superlattice is etched away, allowing a four-lead measurement to be carried out in a well-defined geometry.

dc and ac magnetotransport measurements were performed in a helium cryostat equipped with a 9-T superconducting solenoid. The measurement temperature is $2.0 \pm 0.1\,\mathrm{K}$ and the applied field is always parallel to the substrate plane.

The superlattices structure was thoroughly characterized by low angle x-ray diffraction using a Rigaku rotating anode diffractometer with Cu $K\alpha$ radiation. The specular spectra were fitted with the SUPREX refinement program[17] in order to estimate the layers interfacial roughness. A quantitative structural analysis of the superlattices has been achieved with TEM and high spatial resolution EELS in the cross-sectional geometry. Fe and Cr have similar lattice parameters and also exhibit very close scattering factors for elastic scattering of electrons. Hence conventional diffraction contrast and/or phase contrast imaging in a TEM will neither resolve the layers nor the details of their interface structure. However, energy-filtered imaging using characteristic inner shell excitations[18] make it possible to image the Fe and Cr layers separately and at sufficient resolution to quantify the local structural roughness of the layers. Analytical electron microscopy investigations were carried out using a Philips CM20-FEG TEM equipped with a Gatan imaging filter, capable of obtaining both electron energy-loss spectra and energy-filtered images in real time at high spatial resolution. Samples suitable for imaging by TEM were prepared in the cross-section geometry following the customary treatment of polishing, dimpling, and low angle (less than 10°) ion milling in order to get large electron transparent regions thin enough for investigations by EELS without any multiple scattering.

III. RESULTS AND DISCUSSION

Figures 2(a) and (b) present the low angle x-ray diffraction (LAXRD) specular and nonspecular (rocking curves) spectra taken on a series of superlattices [Fe (3 nm)/Cr (1.2 nm)]$_N$ with $N=20$, 40, 60, grown on top of a 100-nm-thick Nb buffer layer. The rocking curves where measured at a 2θ value of 1°, this ensures high scattered intensity over a wide angular range, and gives information about the layers close to the surface.

Despite the roughness induced by the Nb layer, the specular spectra show clear superlattice peaks up to the second

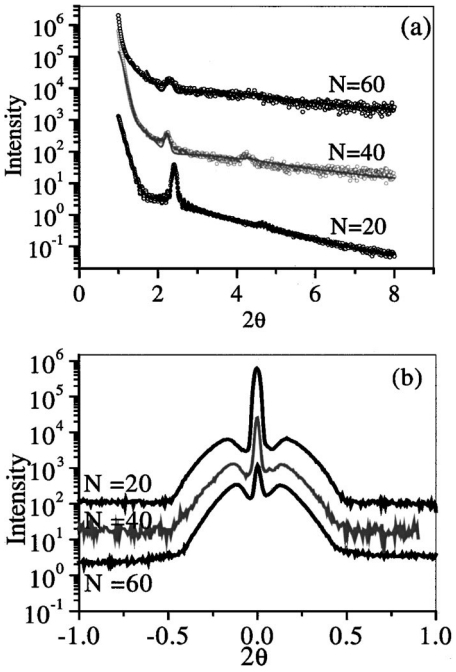

FIG. 2. (a) LAXRD specular spectra taken on a series of superlattices $[\mathrm{Fe}\,(3\,\mathrm{nm})/\mathrm{Cr}\,(1.2\,\mathrm{nm})]_N$ with $N=20$, 40, 60, grown on top of a 100-nm-thick Nb buffer layer. Lines are fits using the SUPREX refinement program; (b) LAXRD rocking curves from the same samples. Spectra are offset for clarity.

order and finite-size oscillations due to the buffer layer thickness for $N=20$. As N increases, the superlattice Bragg peaks broaden and their intensity decreases which indicate that the roughness increases cumulatively with N.[17] The lines in Fig. 2(a) are the fit to the data obtained with the SUPREX refinement program.[17] The structural model assumes a roughness that increases cumulatively with the bilayer index (M) according to a power law $\sigma=\sigma_a M^{\alpha}$ where σ_a is the roughness of the first bilayer, and α an exponent describing the evolution of the roughness. The final values of the fitting parameters were checked to produce minima in the confidence factor of the fit χ^2. The superlattice modulation length $\Lambda=t(\mathrm{Fe})+t(\mathrm{Cr})$ (where t is the layer thickness), extracted from the fit is in good agreement with nominal values derived from deposition rates. The roughness parameters obtained $[\sigma_a=0.37\pm0.02\,\mathrm{nm},\ \alpha=0.4]$, $[\sigma_a=0.37\pm0.02\,\mathrm{nm},\ \alpha=0.4]$, and $[\sigma_a=0.36\pm0.02\,\mathrm{nm},\ \alpha=0.4]$ for $N=20$, 40, and 60, respectively, are in good quantitative agreement implying that the roughness of the first bilayer is the same in all samples (as it should be) and increases cumulatively with the number of layers. Roughness error bars were those producing a 10% increase in χ^2.

Similar results were obtained for a similar series of superlattices grown directly on Si substrates. All the spectra show superlattice peaks up to the third order and the roughness parameters from SUPREX refinement are: $[\sigma_a=0.19\pm0.02\,\mathrm{nm},\ \alpha=0.4]$, $[\sigma_a=0.17\pm0.02\,\mathrm{nm},\ \alpha=0.4]$, and $[\sigma_a=0.17\pm0.02\,\mathrm{nm},\ \alpha=0.4]$ for $N=20$, 40, and 60, respectively. Note that the growth on the buffer layer introduces some additional roughness in the superlattice,[19] i.e., the roughness parameters σ_a, are significantly bigger for the superlattices deposited on top of Nb.

Figure 2(b) shows the rocking curves for samples with 20, 40, and 60 bilayers at a 2θ angle of 1° as a function of the θ offset. The central peak is due to specular scattering and the background is due to nonspecular reflection. It is worth noting that although synchrotron light is usually necessary to ensure high intensity in the nonspecular scattering experiments, the high intensity obtained in our samples with a laboratory x-ray source shows the high degree of correlation of the interfaces from layer to layer (as it will be proven later from EELS experiments). It is known that[20] resonance effects can appear in the nonspecular reflection when the momentum change of incident rays normal to the film, equals a reciprocal-lattice vector and the structure is correlated from layer to layer. Since resonance effects govern the x-ray patterns of the multilayer samples at low angles, obtaining quantitative information usually requires the assumption of self-affine interfaces[21] or a certain growth model.[22] However, it can be qualitatively observed that the ratio of specular to diffuse scattered intensity decreases with N in agreement with an increase of the roughness with the number of layers. Moreover, ''angel wings'' or Yoneda scattering[23] are observed in all three samples. These are due to the increase in the diffuse scattering when θ is equal to the critical angle. Interestingly, angel wings occur at smaller q when the number of bilayers is increased, again pointing to a greater roughness in the vertical direction or to a shorter lateral roughness correlation length.

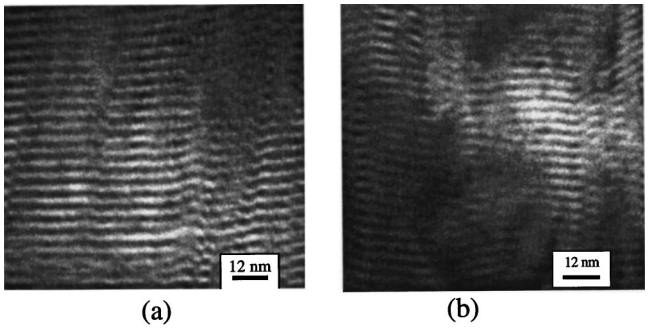

FIG. 3. Cr mapping taken on $[\mathrm{Fe}\,(3\,\mathrm{nm})/\mathrm{Cr}\,(1.2\,\mathrm{nm})]_{60}$ (grown on Nb), (a) on the first 25 bilayers and (b) the last 25 bilayers.

Complementary, quantitative structural analysis of the superlattices has also been obtained with TEM and high spatial resolution energy-filtered imaging in the cross-sectional geometry on the same series of samples. Due to the low contrast in scattering power and similar lattice parameters between Fe and Cr, brightfield TEM pictures taken on these samples show only limited diffraction contrast running along the growth direction indicating a columnar growth of the superlattices.

On the other hand, EELS pictures showed an enhanced contrast. Cr maps using the $L_{3,2}$ edge ($2p$-$3d$ transitions, following dipole selection rules) of the first 25 bilayers and the last 25 bilayers of a $[\mathrm{Fe}\,(3\,\mathrm{nm})/\mathrm{Cr}\,(1.2\,\mathrm{nm})]_{60}$ superlattice (grown on Nb) are shown in Figs. 3(a) and (b), respectively. The first set of bilayers appear much smoother than the last set of layers, indicating a dramatic increase of roughness across the superlattice stack. Note that the roughness is highly correlated. Element (both Cr and Fe) intensity profiles were taken on a series $[\mathrm{Fe}\,(3\,\mathrm{nm})/\mathrm{Cr}\,(1.2\,\mathrm{nm})]_N$ (with $N=20$, 40, 60) along a section perpendicular to the substrate plane with an integration width of 27 nm. These profiles

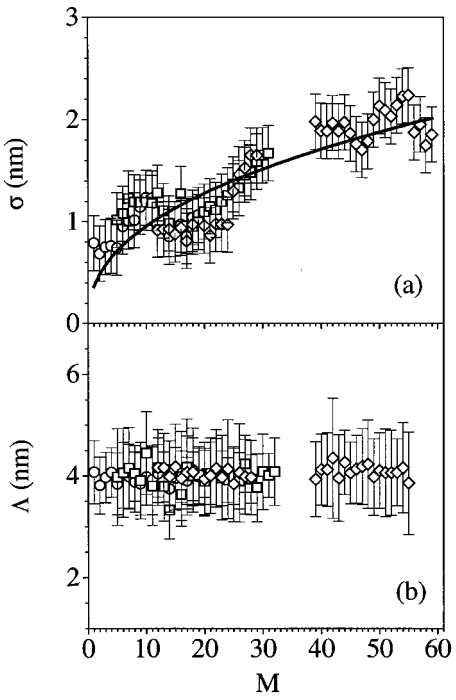

FIG. 4. (a) Roughness of each individual bilayer as a function of the bilayer index M for $N=20$ (○), $N=40$ (□), $N=60$ (◇). Line is a fit to the data with ($\sigma=\sigma_a M^{\alpha}$); (b) superlattice modulation length as a function of the bilayer index M for $N=20$ (○), $N=40$ (□), $N=60$ (◇). Errors bars are the standard deviation of the mean value for each bilayer. Note that the relative error is much smaller that the errors bars of the absolute value of each individual sample.

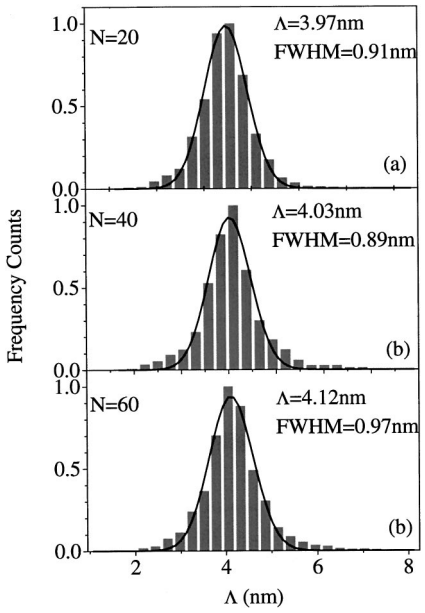

FIG. 5. Modulation length fluctuations for (a) $N=20$, (b) $N=40$, (c) $N=60$.

were taken every 5.4 nm along a 100-nm lateral length (along the multilayer surface). For each Cr (Fe) profile, the position of the maximum EELS intensity was determined. For each bilayer, the roughness is defined as the standard deviation of the Cr intensity maxima over a 100-nm lateral length. Figure 4(a) shows the quantitative roughness of each individual Cr layer inside the superlattice stack for all three superlattices. Note the superposition of the three curves within the error bar margins (given by the spatial resolution of the EELS mapping) and that the roughness increases with the bilayer index. The line is a fit to the cumulative roughness model ($\sigma=\sigma_a M^{\alpha}$) used to extract the roughness parameters from the LAXRD specular spectra. Although the fit is not perfect, the parameters obtained [$\sigma_a=0.36$ nm, $\alpha=0.42$], are very close to the one obtained from the refinement of the LAXRD spectra for $[\mathrm{Fe}\,(3\,\mathrm{nm})/\mathrm{Cr}\,(1.2\,\mathrm{nm})]_N$ grown on a Nb buffer layer.

We have extracted the superlattice modulation length $\Lambda=t(\mathrm{Fe})+t(\mathrm{Cr})$ as a function of bilayer index for the same series of samples by measuring the distance between Cr maxima. As shown in Fig. 4(b), the modulation length is in good agreement with nominal values derived from deposition rates, is completely independent of the bilayer index and therefore insensitive to the dramatic increase of roughness. Note that the relative error on Λ is much smaller than the absolute error bar indicated in the figure for one of the samples.

The statistical histograms in Fig. 5 show the Λ fluctuations for $N=20$, 40, 60. Note that the thickness fluctuations are almost the same for all samples in spite of the increasing roughness. The histograms can be fitted to Gaussian curves (lines in Fig. 5) meaning that the thickness fluctuations are perfectly random. The bilayer thickness fluctuations given by half the full width at half maximum of the Gaussian curves are about 0.45, 0.44, and 0.48 nm for $N=20$, 40, and 60, respectively, which is just about two Fe (or Cr) unit cells. That is additional proof of the roughness correlation. Because the Gaussian fluctuation of layer thickness is also an assumption used in the SUPREX refinement for the intensity calculation of the LAXRD spectra,[17] this result supports the validity of the refinement method of the LAXRD data. Therefore LAXRD and EELS analysis provide roughness parameters in good quantitative agreement and evidence that the roughness is cumulative. Similar results were obtained for the series of superlattices grown directly on Si substrates.

Magnetization measurements were performed on $[\mathrm{Fe}\,(3\,\mathrm{nm})/\mathrm{Cr}\,(1.2\,\mathrm{nm})]_N$ with a SQUID magnetometer at 10 K. Figure 6 presents the dependence of the remnant magnetization (M_R) normalized by the saturation magnetization (M_S) with N. This quantity gives an estimate of the sample fraction which is not antiferromagnetically aligned at 0 field.

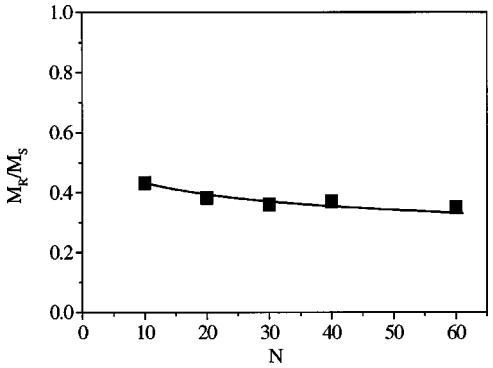

FIG. 6. Remnant magnetization (M_R) normalized by the saturation magnetization (M_S) as a function of the number of bilayers (N). Line is a guide for the eyes.

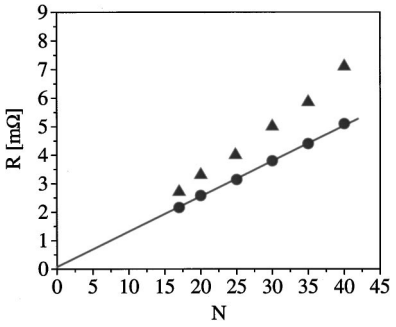

FIG. 7. Perpendicular resistance at 2 K of a series of $[\mathrm{Fe}\,(3\,\mathrm{nm})/\mathrm{Cr}\,(1.2\,\mathrm{nm})]_N$ measured at zero field (squares) and at saturation (triangles). The solid line is a linear fit. Absolute error bars for each sample are about 15% of the measured resistance.

A slight 10% decrease of M_R/M_S is observed with increasing N, over a 10–60 bilayers range. M_R/M_S was estimated to be 0.38 ± 0.02. The relative insensitivity of this ratio to the number of bilayers provides further evidence for the degree of roughness correlation established from structural probes in previous paragraphs.

Because variations of the GMR amplitude have been reported with interfacial roughness for both CIP and CPP geometry,[24–27] we measured the resistance and GMR of a series of $[\mathrm{Fe}\,(3\,\mathrm{nm})/\mathrm{Cr}\,(1.2\,\mathrm{nm})]_N$ superlattices with $10\leqslant N\leqslant 40$ in both configurations. In the perpendicular geometry, the Nb electrodes exhibit a superconducting critical temperature (T_C) of 7.5 K, which is depressed due to the patterning and the proximity with Fe layers.[28] Below T_C, the 100 pillars in series provide a total resistance in the mΩ range, which can be measured with conventional techniques.

Figure 7 presents the perpendicular (CPP) resistance measured at zero field (R_{AP}) and at saturation (R_P) of the series of superlattices. The ''saturation'' field (where ferromagnetic alignment is achieved) is always smaller than the upper critical field of our Nb thin films at 2 K (1.2 T for a 100-nm-thick Nb film). R_P is linear with N, with the Y-axis intercept close to the origin, implying that the contact resistance with the Nb electrodes is negligible. A linear fit through the data gives a Y-axis intercept of $0.05\pm0.1\,\mathrm{m}\Omega$. Note that the error bar is estimated using the error in the absolute value of each measurement. The least-square fit through the data (which gives an intercept of $0.05\pm0.05\,\mathrm{m}\Omega$) indicates that the relative error is much smaller. In any case, this contact resistance is small compared with the intrinsic resistance of our Fe/Cr samples. The intercept corresponds to a contact resistance-cross-sectional area product (2RA) for two interfaces of $1.1\pm2\,\mathrm{f}\Omega\,\mathrm{m}^2$ which is within error bar of other reported Nb-ferromagnetic metal interface resistances.[8,29] A much smaller error is obtained if only the scatter in the data is taken into account ($1.1\pm1\,\mathrm{f}\Omega\,\mathrm{m}^2$). The uniform current distribution in the superconducting Nb electrodes and the negligible superlattice-electrode contact resistance assure that the measured resistance is intrinsic. This is very important in order to obtain independent resistivity and magnetoresistance measurements. The saturation resistivity extracted from the slope of the linear fit is $\rho_P=34\,\mu\Omega$ cm.

Figure 8(a) presents the resistivities ρ_{AP} and ρ_P of $[\mathrm{Fe}\,(3\,\mathrm{nm})/\mathrm{Cr}\,(1.2\,\mathrm{nm})]_N$ in the CPP and CIP geometries for

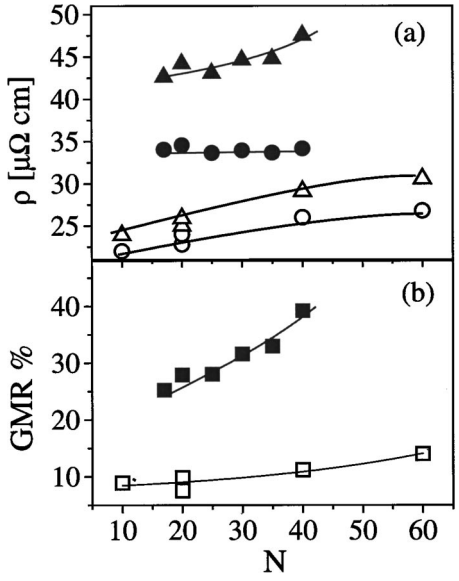

FIG. 8. (a) CPP resistivity ρ_{AP} (▲) of $[\mathrm{Fe}\,(3\,\mathrm{nm})/\mathrm{Cr}\,(1.2\,\mathrm{nm})]_N$, CPP ρ_P (●), CIP ρ_{AP} (△), and CIP ρ_P (○) as a function of N. (b) GMR ratio measured in the CPP (■) and CIP (□) configuration as a function of the number of bilayers.

the two magnetic configurations (P and AP). Figure 8(b) shows the GMR ratio [defined as $(R_{AP}-R_P)/R_P$] of the two series. A first observation is that the CPP resistivity is always larger than the CIP resistivity. Figure 8(a) shows in the CPP configuration a rapid increase of ρ_{AP} with N, while ρ_P stays constant. In the CIP configuration, both ρ_P and ρ_{AP} increase, ρ_{AP} increasing faster.

Figure 8(b) shows that the GMR measured in the CPP configuration is always greater (up to a factor 4) than in the CIP configuration, as predicted[2,5,6] and measured by others.[8,9] The GMR ratio measured in both configurations increases with N. Between 20 and 40 bilayers, the GMR ratio increases by a factor of 1.5 and 1.25 for CPP and CIP configurations, respectively, and shows no sign of saturation.

The increase of the CIP resistivity and GMR with N can be explained by the increase of correlated roughness in the superlattice stack. With increasing N, the correlated roughness becomes high enough to have a substantial contribution from currents flowing across the interfaces. Therefore the measurement configuration become closer to a CAP than a true CIP geometry and the resistivity and GMR are expected to increase with roughness. Note that in the diffusive regime, not only the electrons propagating along the voltage directions contribute to the resistivity. Even for flat interfaces, electrons are scattered and therefore have somewhat random walks, which on the average give a current along the voltage directions. Therefore the current distribution is not uniform and there will always be some electrons crossing the interfaces.

There are two simple extrinsic explanations which can be ruled out as causing the changes in CPP magnetotransport observed here: changes in (i) magnetic coupling and (ii) current flow direction with respect to the interfaces. Magnetic coupling can be ruled out as possible explanation of the magnetotransport changes because: (i) loss of antiferromagnetic coupling (often expected with increased roughness)[24,25]

would decrease the GMR, contrary to what is observed (Fig. 8); (ii) Fig. 6 shows no significant change in magnetic coupling with increasing N (within the range $N=10-40$), and (iii) EELS analysis show that the roughness is correlated without any evidence for an increase in the density of pinholes. The change in current flow direction with respect to the interfaces induced by the high correlated roughness can also be ruled out because it changes the measurement geometry from true CPP to CAP. As a consequence, the GMR would decrease contrary to what is observed (Fig. 8). Therefore a more sophisticated explanation is needed.

A possible explanation for the increase in CPP GMR is the increase of spin dependent scattering with roughness. At saturation, the transport is dominated by electrons of one spin orientation. ρ_P being constant with N indicate that those electrons are weakly scattered by the increasing roughness. On the other hand ρ_{AP} and the GMR increase with N while electrons of both spin direction contribute to the transport. Consequently, the majority electrons are strongly scattered by the interfaces disorder and the correlated roughness acts as a highly spin-selective scattering potential. A similar conclusion was obtained from CIP measurements in Fe/Cr (001) superlattices with negligible bulk scattering[26] and annealing induced interface defects. Note that comparative CIP and CPP measurements place this conclusion on a much firmer footing.

IV. SUMMARY

We have developed a method to measure the perpendicular magnetotransport in metallic superlattices using microfabrication techniques. Because of the minimization of the contact resistance with the electrodes, high number of pillars in series, and the current uniformity in the structures, the method provides simple, direct, and independent access to the superlattice perpendicular resistance and magnetoresistance. CPP and CIP GMR of $[\mathrm{Fe}\,(3\,\mathrm{nm})/\mathrm{Cr}\,(1.2\,\mathrm{nm})]_N$ superlattices were investigated. The CPP GMR is up to four times higher than the CIP GMR and both GMR ratios were found to increase with the number of bilayers (N) as the interfacial roughness increases through the stack. The CIP GMR increase is likely due to an enhanced contribution from currents flowing across the interfaces of the superlattices while the CPP GMR increase is due to an increased spin dependent scattering.

ACKNOWLEDGMENTS

The authors thank Y. Jaccard, A. Fert, and P. Levy for their fruitful comments. This work was supported by the U.S. Department of Energy. J. Santamaria thanks the Fundacion Jaime del Amo and Fundacion Flores Valles for its support. Maria Elena Gómez thanks Universidad del Valle and COLCIENCIAS.

*On leave from Universidad del Valle, A.A. 25360 Cali, Colombia.
†On leave from U. Complutense, 28040 Madrid, Spain.

[1] M. N. Baibich, J. M. Broto, A. Fert, F. Nguyen Van Dau, F. Petroff, P. Etienne, G. Creuzet, A. Friederich, and J. Chazelas, Phys. Rev. Lett. **61**, 2472 (1988).
[2] Y. Asano, A. Oguria, and S. Maekawa, Phys. Rev. B **48**, 6192 (1993).
[3] R. Q. Hood, L. M. Falicov, and D. R. Penn, Phys. Rev. B **49**, 368 (1994).
[4] J. Barnas and Y. Bruynseraede, Phys. Rev. B **53**, 5449 (1996).
[5] P. Zahn, I. Mertig, M. Ritcher, and H. Eschrig, Phys. Rev. Lett. **75**, 2996 (1995).
[6] S. Zhang and P. M. Levy, J. Appl. Phys. **69**, 4786 (1991).
[7] T. Valet and A. Fert, Phys. Rev. B **48**, 7099 (1993).
[8] W. P. Pratt, Jr., S.-F. Lee, J. M. Slaughter, R. Loloee, P. A. Schroeder, and J. Bass, Phys. Rev. Lett. **66**, 3060 (1991).
[9] M. A. M. Gijs, S. K. J. Lenczowski, and J. B. Giesbers, Phys. Rev. Lett. **70**, 3343 (1993).
[10] M. A. M. Gijs, M. T. Johnson, A. Reinders, P. E. Huisman, R. J. M. van de Veerdonk, S. K. J. Lenczowski, and R. M. J. van Gansewinkel, Appl. Phys. Lett. **66**, 1839 (1995).
[11] T. Ono and T. Shinjo, J. Phys. Soc. Jpn. **64**, 363 (1995).
[12] L. Piraux, J. M. George, J. F. Despres, C. Leroy, E. Ferain, R. Legras, K. Ounadjela, and A. Fert, Appl. Phys. Lett. **65**, 2484 (1994).
[13] A. Blondel, J. P. Meier, B. Doudin, and J.-Ph. Ansermet, Appl. Phys. Lett. **65**, 3019 (1994).
[14] K. Liu, K. Nagodawithana, P. C. Searson, and C. L. Chien, Phys. Rev. B **51**, 7381 (1995).
[15] E. E. Fullerton, D. M. Kelly, J. Guimpel, I. K. Schuller, and Y. Bruynseraede, Phys. Rev. Lett. **68**, 859 (1992).
[16] S. S. P. Parkin, N. More, and K. P. Roche, Phys. Rev. Lett. **64**, 2304 (1990).
[17] I. K. Schuller, Phys. Rev. Lett. **44**, 1597 (1980); W. Sevenhans, M. Gijs, Y. Bruynseraede, H. Homma, and I. K. Schuller, Phys. Rev. B **34**, 5955 (1986); E. E. Fullerton, I. K. Schuller, H. Vanderstraeten, and Y. Bruynseraede, *ibid.* **45**, 9292 (1992); D. M. Kelly, E. E. Fullerton, J. Santamaria, and I. K. Schuller, Scr. Metall. Mater. **33**, 1603 (1995).
[18] R. Rennekamp, J. Thomas, B. Arnold, and K. Suenaga, Fresenius J. Anal. Chem. **361**, 621 (1998).
[19] A series of superlattices $[\mathrm{Fe}\,(3\,\mathrm{nm})/\mathrm{Cr}\,(1.2\,\mathrm{nm})]_{20}$ was grown on top of Nb buffer layers with thicknesses varying from 0 to 100 nm. SUPREX simulations of the low angle x-ray spectra show a monotonic increase of σ_a with Nb thickness.
[20] D. G. Stearns, D. P. Gaines, D. W. Sweeney, and E. M. Gullikson, J. Appl. Phys. **84**, 1003 (1998).
[21] S. K. Sinha, E. B. Sirota, S. Garoff, and H. B. Stanley, Phys. Rev. B **38**, 2297 (1988); A. L. Barabasi and H. E. Stanley, in *Fractal Concepts in Surface Growth* (Cambridge University Press, Cambridge, 1995), p. 19.
[22] S. F. Edwards and D. R. Wilkinson, Proc. R. Soc. London, Ser. A **381**, 17 (1982).
[23] Y. Yoneda, Phys. Rev. **131**, 2010 (1963).
[24] J. M. Colino, I. K. Schuller, V. Korenivski, and K. V. Rao, Phys. Rev. B **54**, 13 030 (1996); M. Velez and I. K. Schuller, J. Magn. Magn. Mater. **184**, 275 (1998).
[25] R. Schad, P. Belien, G. Verbanck, K. Temst, V. V. Moshchalkov, Y. Bruynseraede, D. Bahr, J. Falta, J. Dekoster, and G. Langouche, Europhys. Lett. **44**, 379 (1998); R. Schad, P. Belien, G. Verbanck, C. D. Potter, H. Fischer, S. Lefebvre, M. Bessiere, V. V. Moshchalkov, and Y. Brunynseraede, Phys. Rev. B **57**, 13 692 (1998).
[26] R. Schad, P. Belien, G. Verbanck, V. V. Moshchalkov, Y. Bruynseraede, H. E. Fischer, S. Lefebvre, and M. Bessiere, Phys. Rev. B **59**, 1242 (1999).

[27] W. C. Chiang, W. P. Pratt, Jr., M. Herrold, and D. V. Baxter, Phys. Rev. B **58**, 5602 (1998).

[28] G. Verbanck, C. D. Potter, V. Metlushko, R. Schad, V. V. Moshchalkov, and Y. Bruynseraede, Phys. Rev. B **57**, 6029 (1998); Th. Muhge, K. Westerholt, H. Zabel, N. N. Garifyanov, Yu. V. Goryunov, I. A. Garifullin, and G. G. Khaliullin, *ibid.* **55**, 8945 (1997).

[29] C. Fierz, S. F. Lee, W. P. Pratt, Jr., and P. A. Schroeder, J. Phys.: Condens. Matter **2**, 9701 (1990).